JOURNAL OF PROPULSION AND POWER
Vol. 30, No. 1, January–February 2014

Power Deposition into the Discharge Channel of a Hall Effect Thruster

Rafael A. Martinez,* Hoang Dao,† and Mitchell L. R. Walker‡
Georgia Institute of Technology, Atlanta, Georgia 30332

DOI: 10.2514/1.B34897

The deposition of energy into the discharge channel of a 4.5 kW Hall effect thruster from the discharge plasma is investigated. An array of 35 thermocouples is placed along the inner and outer walls of the discharge channel at a spatial resolution sufficient to enable multiple temperature measurement locations within the positive gradient portion of the radial magnetic field profile. Temperature profiles of the inner and outer discharge channels are measured at Hall effect thruster discharge power levels ranging from 0.63 to 2.83 kW, which correspond to peak wall temperatures of 578–813 K. The peak in the wall temperature profile occurs at nearly the same axial location as the peak in the wall radial magnetic field profile. The energy flux from the plasma to the channel walls varies between 0.1 and 90 $W/cm^2 \pm 2\%$ for Hall effect thruster operating conditions from 0.63 to 2.83 kW. Approximately 13 ± 2% of the discharge power is deposited into the discharge channel wall at all Hall effect thruster operating conditions. The average power radiated from the boron nitride discharge channel to the surroundings is approximately 14 + 4/ − 2% of the discharge power at all operating conditions.

Nomenclature

A	=	discharge channel wall area, m^2
I_b	=	beam current, A
I_d	=	discharge current, A
I_{ew}	=	electron current to the wall, A
I_{iw}	=	ion current to the wall, A
κ	=	thermal conductivity, $W\,m^{-1}K^{-1}$
k_B	=	Boltzmann's constant, $J\,K^{-1}$
M	=	proton mass, kg
m	=	electron mass, kg
P_{anode}	=	=anode power, W
P_b	=	base pressure, torr
P_{beam}	=	beam power, W
P_c	=	corrected pressure, torr · Xe
P_d	=	discharge power, W
P_i	=	indicated pressure, torr
$P_{\mathrm{ionization}}$	=	power consumed to ionize propellant, W
$P_{\mathrm{radiation}}$	=	radiated power, W
P_{wall}	=	power into the wall, W
q_{cond}	=	conductive heat flux
q_{rad}	=	radiative heat flux
T	=	temperature, K
T_e	=	electron temperature, eV
U^+	=	ionization potential, eV
V_{cg}	=	cathode-to-ground voltage, V
V_d	=	discharge voltage, V
z	=	axial distance between thermocouples
γ	=	secondary electron yield
ε	=	normal spectral emissivity; energy, eV
η_b	=	beam current fraction
σ	=	Stefan–Boltzmann constant, $W\,m^{-2}K^{-4}$
ϕ_s	=	sheath potential

Received 28 December 2012; revision received 31 May 2013; accepted for publication 20 June 2013; published online 31 December 2013.

*Graduate Research Assistant, Department of Aerospace Engineering, 270 Ferst Dr. NW. Student Member AIAA.

†Undergraduate Student, Department of Aerospace Engineering, 270 Ferst Dr. NW. Student Member AIAA.

‡Associate Professor, Department of Aerospace Engineering, 270 Ferst Dr. NW. Associate Fellow AIAA.

I. Introduction

HALL effect thruster (HET) research and development has increased significantly in the United States over the past 20 years due to the rapid increase of in-space power, global telecommunications, and the realization of commercial and government investment in electric propulsion technology since the early 1960s [1]. There is growing interest in high-power HETs for orbit-raising applications in Earth orbit and deep space missions in support of human application [2]. Military and commercial satellite programs will benefit from the small propellant mass fraction offered by this type of electric thruster [3].

High-power operation of HETs, defined as greater than 10 kW, places elevated demands on thermal management of the design, particularly as power density is increased [4]. The HET thermal state during operation determines largely the discharge channel wall properties, such as secondary electron emission coefficients and sputter yield [4]. Therefore, the thruster temperature characteristics greatly influence HET performance and efficiency by affecting the discharge current and thrust. The overall power deposited to the channel walls is a significant energy loss mechanism in HETs [4–7]. Furthermore, Kim argues that the incident ion power density to the wall is directly proportional to the local erosion rate [6]. The thermal design of the thruster must accommodate the increases in the channel power density to prevent overheating of critical components. Thermal stress experienced by a HET at ignition, shutdown, and overall power deposition in the channel influence the lifetime of the thruster. Therefore, the acquisition of reliable data that quantifies the temperature of HET elements, such as discharge channel walls, metal thruster body, magnetic circuit components, and the hollow cathode body, is crucial for thruster optimization and development of a versatile high-power HET.

Detailed thermal characterization of the discharge channel is obtained through an array of thermocouples. The temperature profile of the inner and outer ceramic channel walls, the ceramic base of the channel, as well as of the anode, are measured as a function of time for various applied power levels. The influences of both the applied voltage and the mass flow rate on the steady-state thruster component temperatures are discussed. In an effort to understand the energy flux from the discharge plasma to the discharge channel wall, radiation and conduction rate profiles are determined as a function of input power and magnetic field along the axial length of the discharge channel. The investigation quantifies power deposition from the plasma onto the discharge channel relative to the magnetic field profile and thruster operating conditions. The calculated energy flux deposited by the plasma onto the discharge channel walls provides improved understanding of energy loss mechanisms inside the channel and refines the overall power balance of a HET. The thermal expansion and thermally induced stresses in high-power HETs pose greater technical challenges compared with low-power devices, due to the physically large size of thruster components. Section II presents a general overview of the power loss mechanisms in a HET. Section III presents the experimental setup. Section IV presents the measured temperature characteristics of the thruster. Finally, Sec. V discusses the results and implications.

II. Power Loss Mechanisms

The dominant power loss mechanisms in an HET are the power deposition to the anode, discharge channel wall, and radial kinetic power of the ions [8]. Energy flux values of $0.1 - 2\ \mathrm{W/cm^2}$ have been measured on the channel walls with a thermal imaging camera, which results in a temperature increase of thruster components [4]. The steady-state power balance equation is

$$P_d = P_{\mathrm{beam}} + P_{\mathrm{radiation}} + P_{\mathrm{wall}} + P_{\mathrm{ionization}} + P_{\mathrm{anode}} \tag{1}$$

where P_d is the discharge power, P_{beam} is the kinetic beam energy, $P_{\mathrm{radiation}}$ is the radiated heat, P_{wall} is the conducted heat, $P_{\mathrm{ionization}}$ is the power required to ionize the propellant, and P_{anode} is the power to the anode due to electron collection. Additional loss terms, such as the power that electrons take into the beam, the ion power to the anode, etc., are relatively small and can usually be neglected [9].

The power put into the plasma is equal to the power that comes out in the form of charged particles and radiation. To the first order, the power injected into the plasma goes into ionization and excitation of neutral gas, the heating of the electrons, and power that is carried to the walls and out the thruster by the ions and electrons. The beam power, or directed kinetic power, of the flight-qualified BPT-4000 is calculated to be 58% of the discharge power (3 kW) using a simple power loss analysis [8]. The other power losses come from various sources related to nondirected kinetic power, ionization, and ohmic heating. In HETs with dielectric walls, the power loss due to electron and ion currents flowing along the radial magnetic field though the sheath to the channel walls P_{wall} represents the most significant power loss.

Using the analysis of Hobbs and Wesson [10] and described by Goebel and Katz [9], the power loss to the dielectric wall of a HET is given by the following formula:

$$P_{\mathrm{wall}} = I_{iw}\left[\left(\frac{2M}{\pi m}\right)^{1/2} e^{e\phi_s/kT_e}\left(\frac{kT_e}{e}\right) + (\varepsilon - \phi_s)\right] \tag{2}$$

where I_{iw} is the ion flux to the wall, M is the proton mass (1.6726×10^{-27} kg), m is the electron mass (9.1094×10^{-31} kg), e is the electron charge (1.6022×10^{-19} C), ϕ_s is the sheath potential, k is the Boltzmann's constant, T_e is the electron temperature in Kelvin, and ε is the ion energy. For the case of space charge-limited secondary electron emission, the sheath potential is $\phi_s = \phi_o = -1.02T_{\mathrm{eV}}$, and the ion energy is $\varepsilon = 0.58T_{\mathrm{eV}}$ to satisfy the Bohm condition. Goebel and Katz calculate the sheath potential for xenon and borosil walls, assuming an average electron temperature along the channel wall of 25 eV, is about -54 V [9]. Substituting these values into Eq. (2) gives

$$P_{\mathrm{wall}} = 45.8I_{iw}T_{\mathrm{eV}} + 2.65I_{iw}T_{\mathrm{eV}} = 48.5I_{iw}T_{\mathrm{eV}} \tag{3}$$

The first term on the right-hand side is the electron power loss to the wall (written in terms of the ion current to the dielectric surface), and the second term is the ion power loss to the wall. The point of this simplified analysis is to show how calculations of the power loss to the channel wall indicate that the electron power to the wall appears to be an order of magnitude greater than the ion power loss to the wall. A common rule of thumb in HETs is that the electron temperature is about one-tenth the discharge voltage [11]. Using Goebel and Katz's analysis [9] and results from Baranov et al.'s SPT-100 calculations [12], the ion current to the wall is approximately 14% of the discharge current.

This radial kinetic power represents a loss of approximately 13% of the discharge power [8]. The power loss to the walls can be estimated from the sheath potentials and electric fields in the plasma edge. Because the wall material is an insulator, the net ion and electron currents to the surface must be equal. However, ion and electron bombardment of common insulator materials, such as boron nitride, at the energies characteristic of HETs produces a significant number of secondary electrons, which reduces the sheath potential at the wall and increases the power loading from the ions. As discussed by Goebel and Katz [9], the total power to the wall of the HET is due to electrons overcoming the repelling sheath potential and depositing an energy of $2T_e$ on the wall plus the ions that have fallen through the presheath potential and then the full sheath potential colliding with the wall.

The power in the beam is given by the following equation:

$$P_{\mathrm{beam}} = \eta_b \eta_v I_d V_d = \eta_v I_b V_d \tag{4}$$

where the current utilization and voltage utilization efficiencies have to be known or evaluated by some means.

The power into the anode can be written as

$$P_{\mathrm{anode}} = 2I_d T_e \tag{5}$$

where the electron temperature in this case is evaluated near the anode. The power to produce the ions in the thruster is the sum of the beam current and the ion current to the walls times the ionization potential:

$$P_{\mathrm{ionizaton}} = (I_b + I_{iw})U^+ = [\eta_b + I_{ew}(1-\gamma)]I_d U^+ \tag{6}$$

where I_{iw} is ion current to the wall, I_{ew} is the electron current to the wall, U^+ is the ionization potential, γ is the secondary electron yield, and η_b is the beam current fraction of discharge current. Neutrals and ions may be excited into higher-level energy states through collisions with electrons. This excitation power is gradually lost through the emission of visible and ultraviolet light as the excited states decay to the lowest energy state. When excited neutrals transition back to the ground state, they radiate their excess energy. A percentage of the power radiated is absorbed by the thruster surfaces and contributes to heating the thruster. However, measurements done by Manzella on the SPT-100 show that less than 0.02% of the total power is lost through excitation power [13]. Therefore, this is neglected in the current analysis. The ionization power represents the power to produce the ions in the thruster and is the sum of the beam current and the ion current to the walls times the ionization potential. This process represents 4–9% of the discharge power [8,9]. Experimentally determined values for $P_{\mathrm{radiation}}$ are discussed later in this paper.

III. Experimental Setup

To obtain accurate measurements of the energy flux deposited by the plasma onto the discharge channel walls and refine the overall power balance of a HET, the experimental design captures detailed in situ temperature measurements along the entire discharge channel wall.

A. Vacuum Facility

All experiments are performed in the Vacuum Test Facility 1 (VTF-1) at the High-Power Electric Propulsion Laboratory (HPEPL). VTF-1 is a stainless-steel vacuum channel 4 m in diameter with a length of 7 m. Two 3800 $\mathrm{ft^3/min}$ blowers and two 485 $\mathrm{ft^3/min}$ rotary-vane pumps evacuate the channel to a moderate vacuum (about 30 mtorr). High vacuum is reached by using six 48 in. diffusion pumps with a combined nominal pumping speed of 155,000 l/s on xenon. The chamber pressure is measured with a BA-571 ion gauge connected to a Varian SenTorr controller with an accuracy of ±20% [14]. The base pressure of VTF-1 for these experiments is 1.5×10^{-5} torr. Figure 1 shows a schematic of the VTF-1.

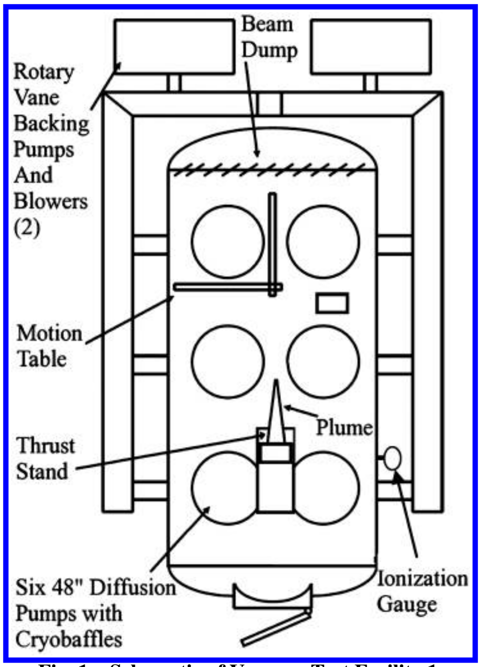

Fig. 1 Schematic of Vacuum Test Facility 1.

B. Hall Thruster

All experiments are performed on a newly built and instrumented Pratt and Whitney Rocketdyne T-140 laboratory-model HET. The T-140 has an outer boron nitride channel diameter of 143 mm, with a nominal thrust of 200 mN at a nominal power rating of 3.4 kW [15]. The discharge channel of the T-140 is made of M26-grade boron nitride. The thruster performance matches the original T-140 HET at multiple points within 3% of published results [15]. Electrical connections enter the channel through separate feedthrough ports. The thruster discharge power supply is protected by a resistor–capacitor filter that consists of a 1.3 Ω resistor in series and a 95 μF capacitor in parallel with the output. The filter acts as a low-pass filter, preventing oscillations in the current over 1.4 kHz from reaching the discharge supply.

A LaB_6 cathode, similar in design to ones used in previous HET testing [11], is located at the 12 o'clock position. The cathode orifice is located approximately 70 mm downstream and 25 mm radially away from the outer front pole piece at an inclination of 30 deg from thruster centerline. For all of the experiments, the thruster is operated for 2–3 h after initial exposure to vacuum conditions to allow for outgassing of the discharge channel walls.

High-purity (99.9995% pure) xenon propellant is supplied to the HET from compressed gas bottles through stainless-steel feed lines. MKS 1179JA mass flow controllers meter the anode and cathode propellant flow. The flow controllers are calibrated before each experiment with a custom fixed-volume apparatus that measures gas pressure and temperature as a function of time, taking into account the effects of xenon compressibility. The mass flow controllers have an accuracy of ±1% full scale. Pressure measurements are corrected for xenon using the known base pressure of air and a correction factor of 2.87 for xenon according to the following equation:

$$P_c = \left[\frac{P_i - P_b}{2.87}\right] + P_b \tag{7}$$

where P_c is the corrected pressure on xenon, P_b is the base pressure, and P_i is the indicated pressure when xenon is flowing into the vacuum channel [16].

C. Surface Thermocouple Attachment

The thermal measurement data reported in the literature are collected with thermal imaging cameras or a few thermocouples located on the discharge channel wall [4,17,18]. This work uses thermocouples (TCs) to measure component temperature to the precise thermal measurement they can record. Thermocouples can obtain accurate temperature measurements of not only the boron nitride channel without affects of foreign material deposition on the walls, but also of thruster components normally hidden from view behind the channel as well. An array of type-K thermocouples inside the ceramic discharge channel are used to measure the temperature as a function of magnetic field, discharge voltage, mass flow rate, and discharge current. TC measurement uncertainty is ±1.1°C. The TCs are spaced at a spatial resolution of 0.01–0.18 in. (0.254–4.572 mm), which is sufficient to resolve the ionization and acceleration regions in addition to the peak gradient of the magnetic field of 232 G/in. (9.13 G/mm) [19].

Figure 2 shows the location of each TC along the inner and outer wall of the HET discharge channel. The TC junctions are placed as close to the plasma as possible to minimize the error due to the heat gradient in the material. A ceramic thickness of 1 mm was chosen as the distance between the TC junction and the plasma. The TC junction is inserted into small holes drilled into the discharge channel walls so that it can stay in place with the assistance of a boron nitride ceramic paste (Aremco Products, Ceramabond 690). Attempts to reduce this distance resulted in occasionally breaking of the material by the drill, which would expose the TC junction directly to the hot plasma. Two TCs are attached to the gas distributor using a combination of ceramic paste (Aremco Products, Ceramabond 571) and fiberglass tape. The TCs are covered in a fiberglass sleeve as they exit the thruster body. Each TC is electrically isolated from ground with an Omega DRF-TCK voltage-isolating signal conditioner positioned outside VTF-1. The signal conditioners are calibrated using a thermocouple simulator with an uncertainty of ±0.25°C.

All of the thermocouples are embedded in the boron nitride channel with the exception of TCs 43 and 44, which are in contact with the gas distributor and therefore at anode potential. TC 43 is attached to one of the gas distributor power studs. TC 44 measures the atmospheric environment in the gap formed between the gas distributor and the discharge channel base. Other thermocouples are located on the outer pole (TC 26), the thruster mounting bracket (TC 28), the thruster backplate (TC 30), and at the base of the inner coil bobbin (TC 49).

Once the thruster thermocouples are connected inside the channel, the data acquisition system continuously records the temperatures. Numerous checks on the thermocouples are initiated before, during, and after testing to verify the functionality of the thermocouples. The thermocouples are checked for proper calibration at not only room temperature, but also using a hot plate that heats the channel to a known temperature. This verifies that the thermocouples are attached properly and increase in temperature at a rate dependent on their placement before channel pumpdown. Magnet warming tests are performed to verify that the thermocouples are behaving normally after pumpdown by increasing the coil currents to typical values used during thruster operation and observing the temperature increase for

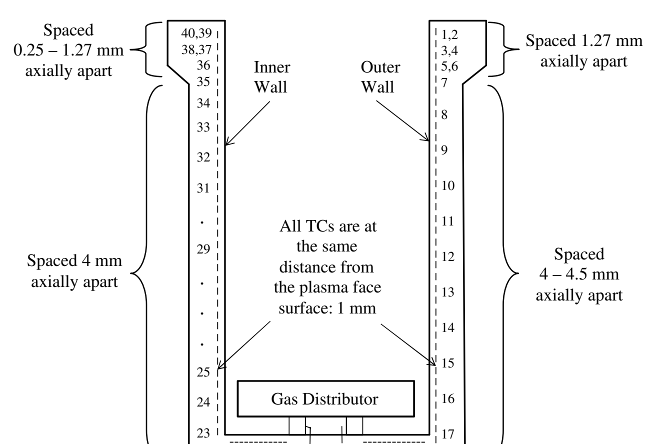

Fig. 2 Thermocouple placement on the T-140 HET.

Table 1 Operating conditions for the T-140 HET power deposition experiment

Operating condition	V_d, V	I_d, A	P_d, W	Anode, mg/s	Cathode, mg/s	Inner coil, A	Outer coil, A	V_{cg}, V	P_c, torr-Xe
1	150.0	4.2	630.0	5.1	0.6	7.9	5.6	−20.2	1.9E-05
2	200.2	4.2	840.8	5.1	0.6	8.4	6.5	−22.8	2.1E-05
3	250.1	4.2	1050.4	5.1	0.6	8.0	6.6	−23.9	1.8E-05
4	300.3	4.3	1291.3	5.1	0.6	7.6	7.6	−25.6	2.1E-05
5	150.1	9.2	1380.9	9.9	1.1	10.0	9.0	−21.1	2.9E-05
6	200.1	9.1	1820.9	10.0	1.1	11.0	8.5	−22.5	2.9E-05
7	250.1	9.0	2250.9	10.0	1.1	11.0	8.5	−23.0	2.9E-05
8	300.2	9.1	2731.8	10.0	1.1	10.5	10.0	−22.9	2.8E-05
9	250.1	7.8	1950.8	8.4	0.9	12.3	11.3	−24.4	2.4E-05
10	250.4	7.4	1853.0	8.4	0.9	10.5	7.5	−23.5	2.5E-05
11	250.1	10.7	2676.1	11.6	1.2	10.9	10.0	−22.2	3.1E-05
12	250.3	11.3	2828.4	12.2	1.0	14.3	13.0	−25.2	3.1E-05
13	150.0	13.3	1995.0	13.8	1.0	12.3	9.0	−21.3	3.2E-05
14	350.2	5.7	1996.1	6.8	1.0	12.3	11.3	−26.6	2.2E-05
15	200.2	10.0	2002.0	11.1	0.9	12.0	8.1	−23.9	2.9E-05
16	200.1	5.1	1020.5	6.0	0.8	9.6	8.0	−25.2	2.1E-05
17	125.2	8.1	1014.1	8.8	1.1	12.5	8.0	−20.5	2.5E-05
18	150.1	6.7	1005.7	7.7	1.0	10.2	7.4	−22.1	2.4E-05

each thermocouple. This isolates the contribution of the magnets to thruster heating. The temperature decay rate upon thruster shutdown is compared with the temperature decay rate from previous thruster shutdowns. To reduce any magnetic field effects to the thermocouple, wire pairs are twisted. In addition, the temperatures of the thruster components were recorded both with and without the thruster magnetic field turned on, and no effects were noticed. Cold gas flow into the thruster after shutdown results in abrupt reductions in temperature, which are recorded with the thermocouples. These steps allow for the identification of thermocouples that are malfunctioning. The electrical isolation of each thermocouple and thruster components is measured with a Megger MIT510/2 insulation resistance tester before shutting the channel door for pumpdown. This allows verification of proper electrical isolation inside the thruster.

IV. Experimental Results

Temperature measurements of the T-140 HET are conducted at xenon mass flow rates of 5.1–13.8 mg/s at discharge voltages of 125–300 V. The magnetic field is optimized for minimum discharge current for each operating point. Thermal drift caused by the thermocouple wires prevented use of the thrust stand. Table 1 shows the operating conditions used in this work. The operating conditions are chosen to investigate the effect of anode mass flow rate, discharge voltage, and magnetic field profile on discharge channel power deposition. At 5.1 and 10 mg/s, testing is performed at discharge voltages of 150, 200, 250, and 300 V. Following this, a study is performed at 250 V and 8.4 mg/s (data points 9–10), which first duplicates a previously published data point condition from Pratt and Whitney Rocketdyne [16] followed by a reoptimization of the magnetic field, which reduces the discharge current by 0.4 A. The reoptimization provides additional insight into the relationship between magnetic field profile and discharge channel temperatures. Data points 11–18 in the test matrix come from the original T-140 test matrix and are duplicated to capture their temperature behavior characteristics and understand the effects of mass flow rate and magnetic field profile.

A. HET Thermal Cycle

Figure 3 shows typical temperature profiles of the T-140 HET startup transient, steady state, and finally through shutdown (thermal decay) for a few select thermocouples on the inner and outer walls. Figure 4 shows temperature data for the discharge channel base, anode, and the outer thruster body as a function of time. The inner magnet is set to 9.6 A and the outer magnet is set to 8.0 A, corresponding to a maximum magnetic field strength of approximately 175 G at a power level of 1 kW. The time range from −1.5 to 0 h shown in Figs. 3 and 4 represents the time taken to condition the external hollow cathode. Thermocouple 26 in Fig. 4 is located directly below the cathode the outer pole. The temperature of TC 26 increases rapidly at the −0.5 h mark due to thermal radiation from the cathode body. Thruster ignition occurs at 0 h in the figures. It takes 3.5 h for the inner wall of the discharge channel to reach thermal equilibrium (defined as a change in temperature of less than 1 K/min), whereas the outer wall of the discharge channel requires 4.5 h to reach thermal equilibrium. The gas distributor power stud does not reach thermal equilibrium even after 5 h. The HET thermal cycle test shown in Figs. 3 and 4 is conducted to determine how long to wait at each operating condition for the thruster to be at approximately 95% of thermal equilibrium, which is the temperature used for this study. Based on the 1 kW condition, this occurs 1.5 h after thruster ignition. The maximum heating rates for the inner and outer walls are 47 and 134 K/min, respectively. The maximum cooling rates for the inner and outer walls are 42 and 43 K/min, respectively.

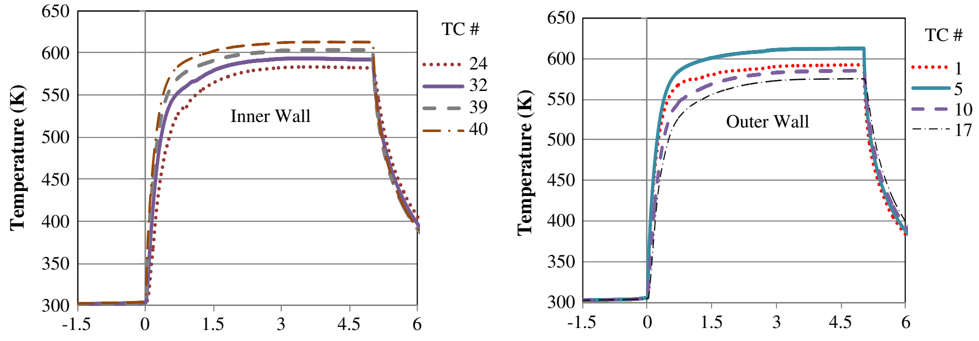

Fig. 3 Temperature history of inner and outer wall at the 200 V, 5.1 mg/s operating condition.

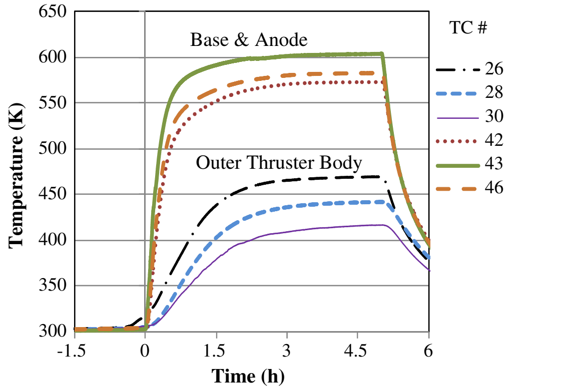

Fig. 4 Temperature history of the anode, base, and various thruster body locations at the 200 V, 5.1 mg/s operating condition.

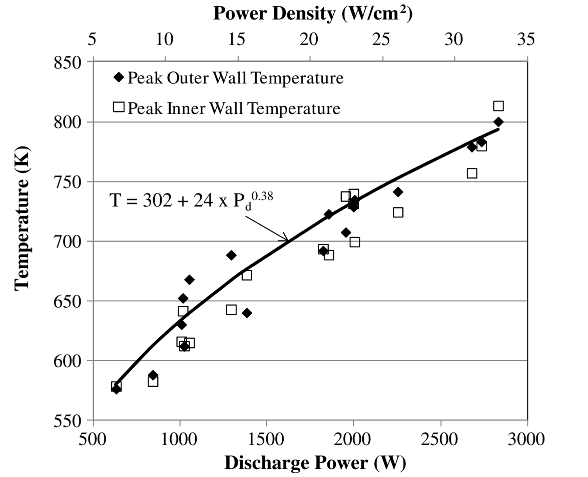

Fig. 6 Peak inner and outer discharge channel wall temperatures as a function of the T-140 HET discharge power.

Figure 5 shows the temperature distribution on the BN discharge channel at thermal steady state for the 200 V, 5.1 mg/s operating condition. The thick black border that surrounds the outer surface of the discharge channel represents the titanium radiation shield foil. The outer wall radiation shield is in direct contact with the thruster body. The thicker piece of the radiation shield on the outer wall is in direct contact with the thruster body. The inner radiation shield is in contact with the discharge channel. The inner radiation shield is not welded to the rest of the radiation shield structure around the discharge channel, which means that there is not a good conductive path to transfer the heat away from the inner wall and lower the temperature.

The temperature variation on the outer wall is due to the combination of the radiation shield making direct contact with the thruster body at the 46 mm axial location and the final upstream 12.7 mm section of the outer wall making rough contact with a separate component of the magnetic circuit. Both locations provide a direct heat transfer path to the rest of the thruster. The inner wall temperature has a temperature gradient of 24 K between the axial distances of 47–51 mm along the wall in Fig. 5. This location corresponds to not only the end of the titanium radiation shield on the inner wall, but also the maximum inner wall radial magnetic field strength location.

Steady-state temperature data for the thruster discharge channel are obtained for every test point tabulated in Table 1. These temperature data are used to obtain the peak temperatures of the inner and outer walls. Figure 6 shows the peak equilibrium inner and outer wall temperatures of the T-140 HET as a function of discharge power. The power density in Fig. 6 is calculated using the thruster channel area. For each test point, the magnetic field is reoptimized for minimum discharge current. Mazouffre et al. [20] show that the relation between the discharge channel wall temperature and the discharge power can be written as $T = a + b \times P_d^n$, where a is the temperature of the wall when the thruster is not operated, b depends on wall material and the geometry, and the exponent n is solely connected with the material. Mazouffre et al., using the PPSX000-ML HET with an infrared camera, obtained the following expression: $T = 270 + (23 \pm 5) \times P_d^{(0.38\pm0.02)}$ [20]. It is worth noting that Mazouffre et al. tested their HET with a BN-SiO_2 channel, whereas the T-140 HET uses M26-grade boron nitride (a similar material). Figure 6 shows that the expression fits the T-140 HET temperature distribution with an R^2 value of 0.9993. The expression indicates that the material has a strong impact on wall temperature. Material properties such as electrical conductivity, secondary electron yield, and sputtering rate determine plasma sheath properties, which in turn influence discharge behavior. Moreover, the thermodynamic coefficients of thermal diffusivity and emissivity govern the loss rate of thermal energy from the material. These values are in agreement with the ones obtained with other HETs of similar size and power level [17]. The peak inner wall temperature point above the curve fit at 2828 W is at the single data point taken at the maximum mass flow rate of 12.2 mg/s. These observations are further analyzed in Sec. V.

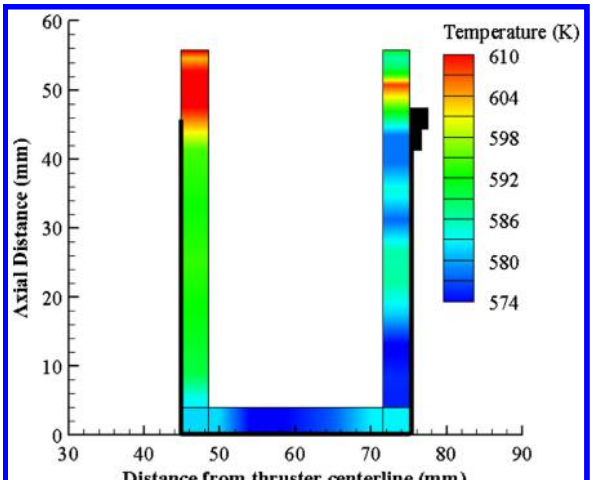

Fig. 5 Discharge channel wall temperature distribution at the 200 V, 5.1 mg/s operating point at thermal steady state.

B. Influence of Propellant Mass Flow Rate

A study of the influence of the injected xenon mass flow rate upon the thruster temperature profile is performed. Figure 7 shows the typical temperature profile of the inner wall of the T-140 discharge channel at 250 V for the 5.1 and 10 mg/s flow rates. Figure 8 shows the temperature profiles of the outer wall at 250 V for the 5.1 and 10 mg/s flow rates. Comparison of Figs. 7 and 8 shows that doubling the anode mass flow rate from 5.1 to 10 mg/s doubles the temperature difference between the thermocouples located above and below the downstream end of the radiation shield at an axial distance of approximately 46 mm. As expected, the temperature increases with the injected xenon mass flow rate due to an increase in both the number of ions and the number of electrons produced inside the channel and the corresponding power loss to the walls from those ions and electrons.

Measurements of channel temperature with time are also conducted to shed further light on HET thermal characteristics. The reduction in the magnetic field strength when going from 10 to 5.1 mg/s results in a reduction of the magnetic field gradient, causing a shift of the acceleration zone further back into the channel. This acceleration zone shift means that ions are accelerated further upstream, causing the plasma to begin depositing energy further upstream in the discharge channel wall, which results in a smaller temperature difference along the distance between the channel base and downstream end thermocouples. This trend is more clearly seen

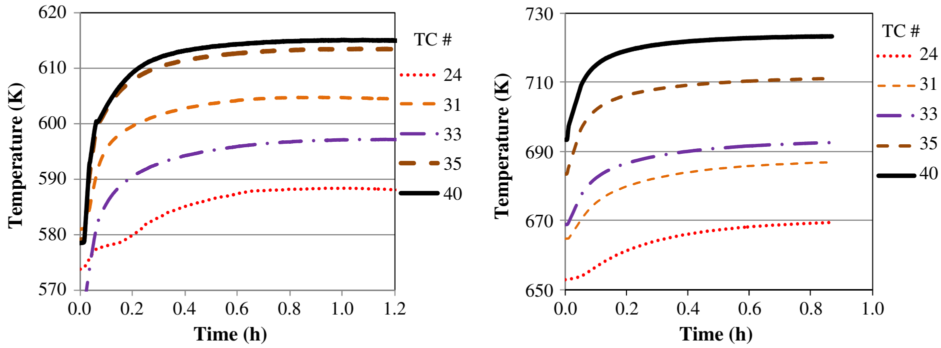

a) Inner wall at 5.1 mg/s

b) Outer wall at 10 mg/s

Fig. 7 Inner wall temperature profiles as a function of time at 250 V.

in the outer wall as the peak temperature moves much further upstream when going from 10 to 5.1 mg/s. These observations are discussed further in the next section. The increase in temperatures as the mass flow rate is doubled is not unexpected. Higher mass flow rates tend to lead to higher numbers of ions and electrons created that can hit the walls. In this case, doubling mass flow rate (hence doubling the input power from 1 to 2 kW) increases the temperatures by approximately 14–18% on the inner wall and 10% on the outer wall. However, only increasing the mass flow rate cannot distinguish between the effects of electrons and ions on wall heating because the propellant mass is constant for this study. Discharge voltage variation can shed more light on the dominating heating mechanisms, and this is discussed in the next section.

V. Discussion

Even if 50–70% of the electric input power to a HET is converted into thrust, the power losses to the wall of the discharge channel and to the anode are significant. Therefore, a more detailed analysis of the collected thermocouple data is done to quantify the thermal behavior of a HET. First, the discussion will relate the temperature and heat flux calculations to the HET magnetic field topography. This is followed by an examination of the temperature characteristics of the HET as a function of discharge voltage. The time-resolved thermocouple measurements are then used to shed light on the origin of the energy flux deposited by the plasma onto the discharge channel surface. Finally, the radiation from the boron nitride channel to the environment is calculated. As shown in Eq. (1), the determination of the wall losses can allow for an estimate of the anode efficiency through the calculation of the beam energy.

A. Influence of Magnetic Field Topography

An investigation is conducted to study the relationship between the magnetic field profile and the wall temperatures. Figure 9 shows the temperature profile at 250 V, 8.41 mg/s with two different magnetic field shapes. TCs 38 and 40 on the inner wall and TCs 2 and 4 on the outer wall are located on the downstream portion of the discharge channel wall, near the exit plane. The rest of the TCs cover the upstream portion of the channel. The initial magnetic field setting (B-field 1) is based on the Pratt and Whitney Rocketdyne published T-140 HET test matrix [16]. Once the thruster reaches approximately 90–95% of thermal equilibrium, the magnetic field is reoptimized for minimum discharge current (B-field 2). The inner coil decreases from 12.3 to 10.5 A and the outer coil decreases from 11.3 to 7.5 A. The discharge current drops by 0.4 A and the discharge current-to-mass flow rate ratio decreases from 0.93 to 0.89 A/mg/s. Figure 9 shows that the inner wall temperatures all decrease with the larger reductions occurring further downstream along the inner wall, whereas only the downstream thermocouples in the outer wall show a temperature increase. The upstream outer wall thermocouples show a decrease in the temperature (Fig. 9b). Analyses of the magnetic field changes using Infolytica's Magnet software program reveal that there is a reduction in the inner wall peak magnetic field of 60 G and a reduction of 45 G for the outer wall peak magnetic field (a 15–20% drop in wall field strength). A reduction of 37 G occurs with the centerline peak magnetic field. Locations of the peaks in the centerline and wall fields remain unchanged. An observation of the upstream portion of the discharge channel temperatures in Fig. 9 shows that both the inner and outer wall temperatures decrease nearly the same amount.

Analysis of the data from Fig. 9 shows that the radiated energy loss drops by 10% for the second optimized magnetic field settings. However, because the mass flow rate remains constant, the drop in discharge current (0.4 A) results in a 5% drop in discharge power level (5% drop in power density). Therefore, the radiated energy loss-to-discharge power ratio decreases by only 1%. Close examination of the magnetic field line contours shows that the magnetic field line that connects the outer wall to the furthest downstream portion of the inner wall shifts upstream along the outer wall by 1.27 mm. This alteration causes a slight tilting of the plasma plume outward, which exposes a larger portion of the downstream half of the outer wall to the high-energy ions. Note that the temperatures of the upstream half

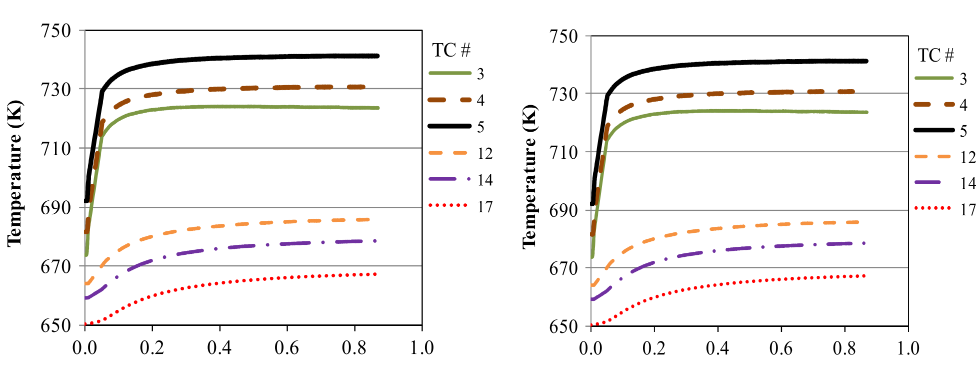

a) Outer wall at 5.1 mg/s

b) Outer wall at 10 mg/s

Fig. 8 Outer wall temperature profiles as a function of time at 250 V.

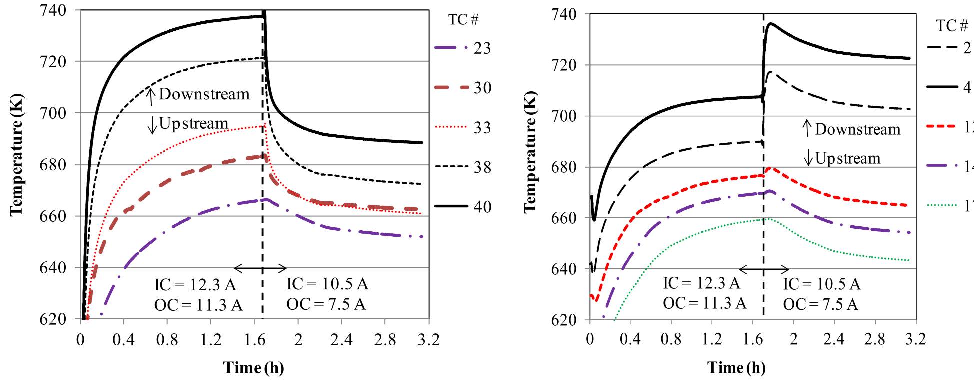

a) Inner wall b) Outer wall

Fig. 9 Inner and outer wall temperatures as a function of two different magnetic field settings at 250 V, 8.41 mg/s operating condition. IC, inner coil; OC, outer coil.

of the inner and outer walls remain nearly identical to each other for both magnetic field settings (670 ± 10 and 655 ± 10 K). This points to ion bombardment as the primary source of wall heating, instead of electrons, because the ions are located in the downstream half of the channel [21].

Figure 10a compares the inner wall magnetic field and the inner wall temperature distribution for the thruster operating at 250 V, 8.41 mg/s. For clarity, only the magnetic field lines for the first magnetic field setting (B-field 1) are shown because the values of the curve for B-field 2 are only slightly less than those of B-field 1. As can be seen in Fig. 10a, for both magnetic field settings, the inner wall temperature begins to increase rapidly soon after the inner wall field begins to increase. The inner wall magnetic field peaks at the channel exit plane (45 mm axial location in Fig. 10). The wall temperature continues to increase all the way down to the exit of the channel.

Figure 10b shows the outer wall magnetic field compared with the outer wall temperature at the 250 V, 8.41 mg/s operating condition. Only the magnetic field curves for the first magnetic field setting (B-field 1) are shown for clarity because the curve for B-field 2 is merely shifted downward. Although the inner and outer wall profiles are very similar, the radial magnetic field peaks earlier along the outer wall by approximately 5.5 mm. It appears this provides enough material distance to allow the outer wall temperature to reach its peak and then decrease due to the decrease in the magnetic field along the outer wall. In addition, the magnetic field along the outer wall transitions into the negative field region for a sufficient amount of time to cause a similar trend in the outer wall temperature profile slightly further downstream. There appears to be no direct correlation the wall temperatures and the centerline magnetic field profile.

The peak temperatures in Fig. 10b do not correspond to the furthest downstream thermocouples for the outer wall of the discharge channel. Measurements of the centerline magnetic field strength indicate that the acceleration zone begins approximately 8 mm upstream of the exit plane of the channel. However, magnetic field plasma lens effects can cause the acceleration zone along the walls to be slightly further downstream relative to the channel centerline [22]. This provides additional evidence for the maximum wall temperature location corresponding to the beginning of the local acceleration zone. The observed asymmetry in the magnetic field profiles along the inner and outer walls (Figs. 10a and 10b) is therefore consistent with the acceleration zone occurring further upstream along the outer wall.

When the peak in the magnetic field along the inner wall is upstream of the discharge channel exit plane, this results in a slight peak of the inner wall temperature profile upstream of the discharge channel exit plane. The correlation between the magnetic field along wall and the measured temperature along the wall represents the first experimental verification of this relationship. However, it is still difficult to distinguish between whether the dominant heating mechanism is due to ions or electrons. The peak temperature measurements are located where magnetic field lines with high-temperature electrons contact thruster surfaces [23]. Recent thermal simulations conducted also point to the strong correlation between inner and outer wall field profiles and the distribution of the power deposition on the walls [24]. In addition, stronger magnetic field strength results in a greater plasma resistivity, to maintain the current through the thruster, the local electric field must increase. This tends to be associated with a plasma potential drop, so the location of the peak in magnetic field is correlated with the location of the acceleration zone. The location of the rapid rise in temperature of the wall can be thought of as another indication of the acceleration zone

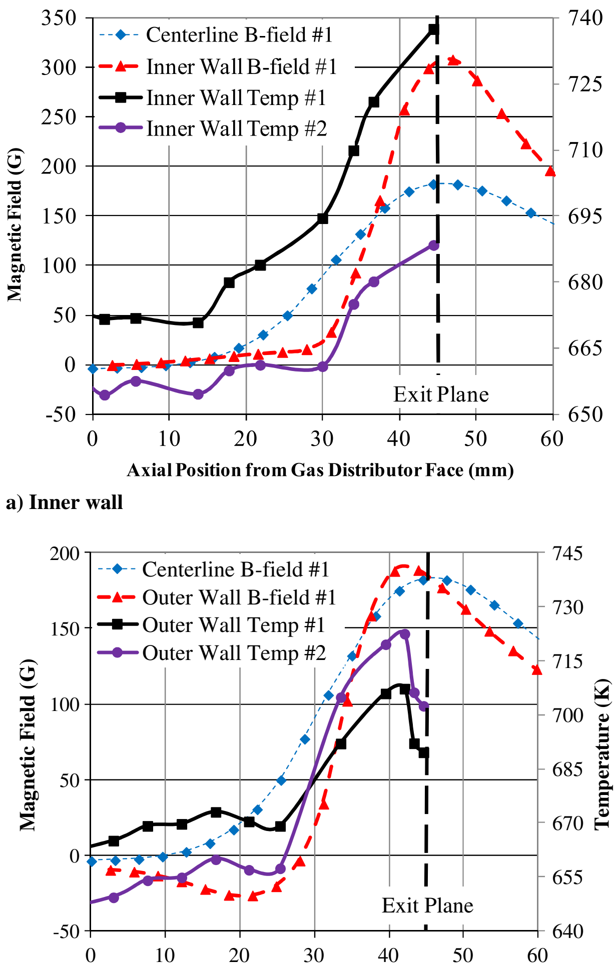

b) Outer wall

Fig. 10 Radial magnetic field and temperature comparison at the 250 V, 8.41 mg/s operation condition. B-field 1: IC = 12.3 A, OC = 11.3 A; B-field 2: IC = 10.5 A, OC = 7.5 A.

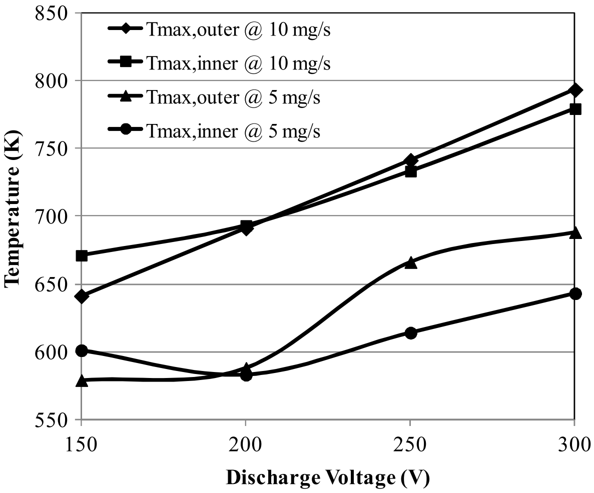

Fig. 11 Peak inner and outer wall temperatures as a function of discharge voltage at anode mass flow rates of 5.1 and 10 mg/s.

beginning. In addition, because the peak magnetic field occurs near the beginning of the acceleration zone near the exit plane, this region is subject to large wall power losses from high-energy electrons as well as high-energy beam ions. The maximum electron temperature occurs near the channel exit in the region of strongest magnetic field where the Hall current is at maximum. Therefore both electrons and ions tend to have their largest impact on the walls near the peak of the magnetic field. As will be discussed in the next section, the electron temperature variation reveals the dramatic impact of electron heating on HET thermal characteristics.

B. Impact of Discharge Voltage

Figure 11 shows the trends in the peak inner and outer wall temperatures for anode mass flow rates of 5.1 and 10 mg/s over a discharge voltage range of 150–300 V. The ion energy, as well as the flux of ions and electrons impinging onto the discharge channel walls, increases with voltage. As is discussed in Sec. V.A, the magnetic field lines are tilted away from the thruster centerline for every operating condition such that, as the voltage increases, higher energy ions impact the walls due to the radial electric fields, which yield an increase in wall temperatures.

Below a discharge voltage of 200 V, the inner wall temperature is up to 30 K hotter than the outer wall. Typically, at discharge voltage below 200 V, the anode efficiency of the HET drops and the acceleration zone moves downstream, which results in higher beam divergence and a great number of ions hitting the discharge channel walls. The lower mass flow rate can also impact the ionization zone by moving it downstream, which causes the ions to be accelerated later in the acceleration zone and further increases the beam divergence.

Above a discharge voltage of 200 V (for both mass flow rates), the outer wall can be as much as 50 K above the inner wall temperature. At these higher voltages, the impact of the ions on the walls is more severe due to the rapid rise of the ion energy and the radial electric fields caused by the tilting of the magnetic field outward. As the discharge voltage is increased, the acceleration zone recedes further into the channel, causing the ions to fall through a larger portion of the total acceleration voltage, and the walls are therefore exposed to higher beam energies. There is also a 70–100 K difference for the outer wall and a 110–125 K difference for the inner wall between the 5.1 and 10 mg/s curves if one looks at the inner and outer wall temperature curves. The improved plume divergence at the higher voltages and mass flow rates shifts the impact of the high-energy ions to the downstream portion of the outer walls. However, the electrons can still play a large role in the heating of the walls. Upstream of the acceleration zone, the electrons are highly concentrated at low energies due to the low temperature and near-Maxwellian structure. Once the acceleration zone is reached, the electrons heat up significantly and obtain energies several times higher than in the region upstream.

An additional study is conducted to make a more direct comparison between the effects of the discharge voltage and mass flow rate on the wall temperature profiles. In this study, the discharge current remains constant at 8 A, but the discharge voltage increases from 125 to 250 V. The inner magnet current remains unchanged, but the outer magnet is decreased by 3 A when going from 250 to 125 V. Doubling the discharge voltage results in a 20% increase of the peak temperature of the inner wall and a 15% increase in the peak temperature of the outer wall. These percentage increases are approximately the same as what is noticed by increasing the mass flow rate to double the input power. As flow rate is increase, the propellant utilization typically increases because the ion production rate is directly proportional to the neutral density, which is proportional to mass flow rate [25]. The temperatures of the walls seem equally sensitive to an increase in the ion production as it is to an increase in beam energy. However, the number of ions produced needs to be quantified to confirm this. Interestingly, at the 250 V and 8.41 mg/s condition, the differences between the highest and lowest temperatures on the inner and outer walls are approximately 343 K. At the 125 V and 8.41 mg/s condition, the difference between the highest and lowest temperature is 284 K for the inner wall and 310 K for the outer wall. This could be an indication of more ions being born in areas of radial electric fields at the lower voltages, which results in a greater number of ions hitting the upstream part of the discharge channel walls. Although the effect of the radiation shield, to transfer heat away from the channel walls, is not seen at the 125 V, 8.41 mg/s condition, it is very noticeable for the outer wall at the higher power level. The gas distributor power stud temperature is approximately the same for both operating points, 673 K. At low voltages, higher divergence of ions is typically noticed within the channel [26]. This will cause more ions (albeit lower energy ions compared with the 250 V case) to hit the walls, leading to elevated temperatures further upstream of the acceleration zone, explaining the smaller temperature gradient when going from the base of the channel to the exit plane as the voltage decreases.

Figure 12 summarizes the experimental temperature data for the inner and outer walls at discharge voltages of 150, 200, 250, and 300 V for anode mass flow rates of 5.1 and 10 mg/s. At 10 mg/s, the temperature trends as a function of voltage are linear in contrast to the step-like trend seen at 5.1 mg/s. Figure 12a highlights the growing temperature separation between the thermocouples downstream and upstream of the radiation shield end with voltage at the 10 mg/s case. As the voltage increases, the energy of the ions increases and most of the power is delivered to the downstream end of the outer wall, whatever the propellant mass flow rate. If we assume an acceleration voltage of 200 V and an ion divergence angle of 30 deg off centerline, the resultant maximum radial energy would be 100 V. This points in favor of a power deposition mechanism dominated by ion impact instead of electron impact on the final section of the wall [17]. Close examination of the 5.1 mg/s curves in Fig. 12b shows a much smaller temperature separation, but like the 10 mg/s case, it continues to grow with voltage. With a constant propellant supply, increased voltage creates more energetic electrons with energy approximately one-tenth the voltage.

To estimate the impact of losses associated with particle interactions, an analysis conducted by Xu on the T-220HT of ionization, electron–ion recombination, and ion–wall neutralizations is reviewed and shows that 13% of the ions are lost to wall neutralizations, for the conditions similar to the T-140 HET [21]. Electron–ion recombination collisions are a negligible contribution to ion losses in the thruster, accounting for only 2×10^{-15} A of ion current. It should be mentioned that the surface area assumed in the calculations is based on the assumption of no ions at the wall upstream of $0.5L_C$, where L_C is the channel length. The assumption is based on internal measurements of HETs [21,22].

To examine the effect of thruster operation on losses of power due to plasma–surface interactions, the channel wall temperature-to-discharge power ratio is plotted as a function of discharge voltage. The ratio allows one to quantify the amount of power deposited onto walls per unit electrical power. This ratio is calculated using the peak

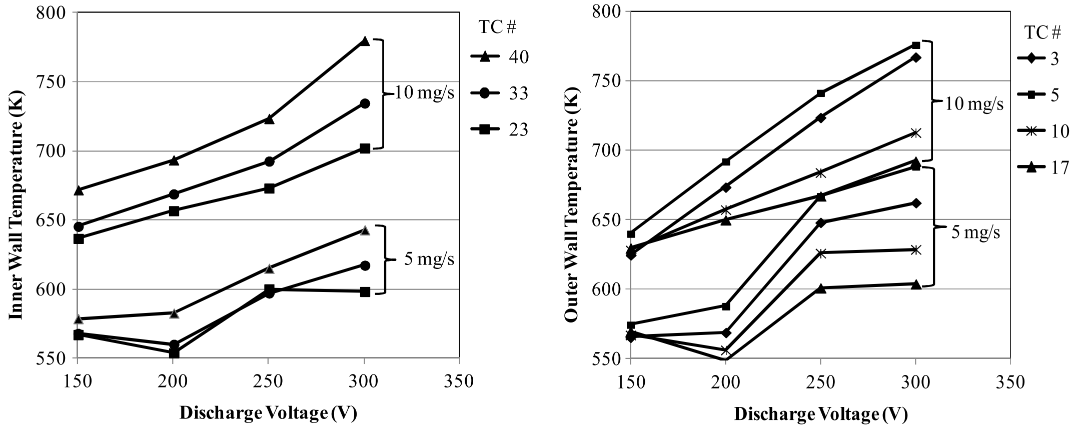

a) Inner wall temperature

b) Outer wall temperature

Fig. 12 T-140 HET wall temperatures as a function of discharge voltage at 5.1 and 10 mg/s.

inner and outer wall temperatures for each operating condition as well as an average wall temperature defined as

$$T_{\text{wall}} = \frac{T_{\text{outer}} + T_{\text{inner}}}{2} \tag{8}$$

where T_{outer} is the outer wall temperature and T_{inner} is the inner wall temperature. The two measured temperatures correspond to the mean recorded temperature in the final ~20 mm section of the channel where most of the energy is deposited into the wall. This value is also used to make comparisons with work done by Mazouffre et al. [17].

Figure 13 plots this value as a function of discharge power for the T-140 HET. The ratio varies in a smooth way over a broad range of applied powers. The curve shape indicates that the amount of power deposited onto the walls per unit of discharge power is certainly lower at the high power. It implies a better utilization of energy for ionization and/or acceleration purposes at the high-power level. This experimental result agrees with the fact that, for a given HET design, the thrust efficiency tends to increase with the discharge power. The evolution of the wall temperature-to-power ratio reveals that the wall temperature, and therefore the power losses, is not sensitive to thermal history of the thruster or material surface conditions.

Comparisons with the SPT-100 and PPS-1350-G HETs from the work done by Mazouffre et al. [17] show that the T-140 curve is clearly shifted downward compared with those thrusters at the same power levels and mass flow rates. This could be an indication of the improved thermal management design of the T-140 HET. However, an alternate explanation is simply a size effect because the smaller surface-to-volume ratio of the T-140 HET reduces wall losses.

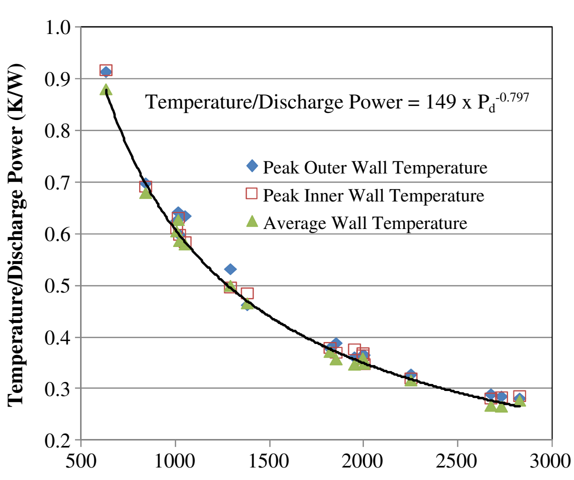

Fig. 13 Ratio of the peak and mean channel wall temperatures to discharge power as a function of the discharge power for the T-140 HET.

C. Plasma Power Deposition to the Wall

The temperature map of the thruster is actually a balance between the conduction of energy along the channel wall, radiation thermal losses of the thruster walls to the environment, and the energy fluxes from the plasma (radiation and particle interactions through the plasma sheath) in the discharge channel. HETs operate in a rarefied environment and the plasma inside the channel is at a low pressure (typically 1 Pa). Consequently, convective heat transfer is neglected [4]. For the steady flow of heat across a plane wall (see Fig. 14) with surfaces at temperatures of T_1 and T_2, where T_1 is greater than T_2, the heat flow Q per unit area of surface A (the heat flux) is

$$\frac{Q}{A} = q_{\text{cond}} = k\left(\frac{T_1 - T_2}{Z_1 - Z_2}\right) = k\frac{\Delta T}{\Delta z} \tag{9}$$

The thermal conductivity k is assumed a constant over the temperature ranges reported in this article for the boron nitride channel material, 29 W/m · K.

At thruster ignition, constant localized power deposition from the plasma to the wall (near B_r maximum) and heat conduction through the BN material are the processes that dominate the shape of the temperature profile along the BN channel wall. In addition, at the low BN wall temperatures observed at thruster ignition, the radiative energy losses are negligible. With these observations, one can calculate the profile of heat flux from plasma to the wall in the axial direction along the wall. For example, in Fig. 8, the thruster reaches the 250 V, 10 mg/s operating point at approximately 3.2 min. At this time, the temperature gradient between a pair of thermocouples (spaced a distance Δz) is calculated. To obtain the conductive heat flux between TCs 1 and 2 (see Fig. 14), the temperature difference and the distance between the two TCs ($\Delta z = 0.05$ in., 1.27 mm), is used in Eq. (9). The area A is based on the area of an annulus representing each wall and the thickness of the channel wall (the outer wall in the case of Fig. 14). The assumption is that, for a particular axial location, the temperature is constant about the circumference of the channel. Previous temperature measurements of HET discharge channels support this assumption [17,27,28].

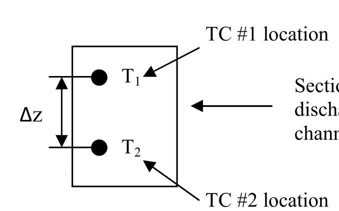

Fig. 14 Schematic of nomenclature used for heat conduction calculations along the channel walls.

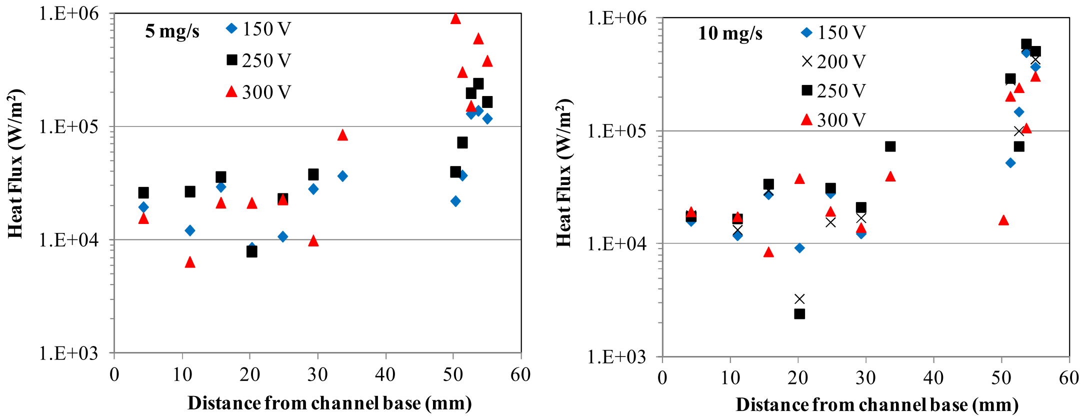

a) Mass flow rate at 5.1 mg/s b) Mass flow rate at 10 mg/s

Fig. 15 Conductive heat flux along the discharge channel wall for the T-140 HET on the outer wall at 5.1 and 10 mg/s.

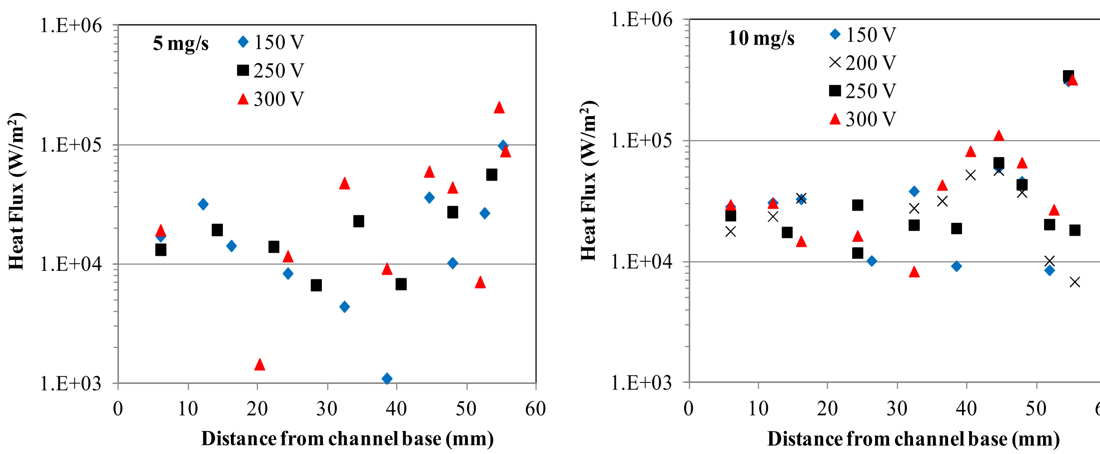

a) Mass flow rate at 5.1 mg/s b) Mass flow rate at 10 mg/s

Fig. 16 Conductive heat flux along the discharge channel wall for the T-140 HET on the inner wall at 5.1 and 10 mg/s.

Figures 15 and 16 show the measured conductive heat flux through the boron nitride channel at 5.1 and 10 mg/s. The location of the maximum conductive heat flux value along the channel wall denotes the location of the maximum energy flux from the plasma to the channel wall. As expected, the maximum conductive heat flux values are near the end of the discharge channel, where the ions with the highest energy levels impact the wall [4,29]. Ions are strongly accelerated at the channel outlet where the axial electric field is high [30]. Calculations done by Shastry of the incident ion power density from wall-mounted Langmuir probe data indicate that the profile of net power density deposited to the channel wall is a combination of the decrease in ion current density and the increase in ion energy as the exit plane is approached [22].

The power loss from the plasma to the channel wall is determined from the maximum heat flux values in Figs. 15 and 16 for each voltage. The sum of the outer and inner walls is used to calculate the total power loss from the plasma to the wall. For example, Fig. 16a shows that, at the 630 W power level (150 V, 5.1 mg/s), the peak heat flux from the plasma to the inner wall is approximately 98,000 W/m^2. This value is multiplied by the area between the corresponding thermocouples used to calculate this heat flux value (TCs 39 and 40) which is 4.78×10^{-4} m^2 and results in a power loss from the plasma to the inner wall of 47 W. A similar procedure is used for the outer wall and the sum of the two walls is added to obtain the total power loss from the plasma to the wall (78.34 W in this case or 12% of the discharge power). Figure 17 shows that power deposition to the wall from the plasma is a strong function of discharge power. Figure 17 shows that the power deposited into the wall from the plasma can be approximated as a linear function of discharge power ($0.125 \times P_d$). The average percentage of discharge power deposited into the wall from the plasma for the T-140 HET is approximately 13% over the entire power range tested. This percentage has an uncertainty of ±2%. The percentage is higher for the lowest voltages tested (125 and 150 V), likely due to the higher beam divergence typically seen with these lower voltages [21].

Shastry's internal wall-mounted probe data are used to calculate the ion power deposition, but neglects the contributions of electrons

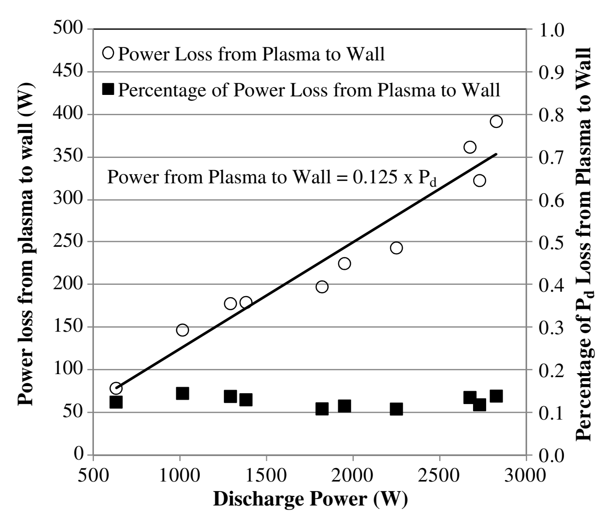

Fig. 17 Power deposited into the wall from the plasma and percentage of discharge power deposited into the wall from the plasma as a function of discharge power.

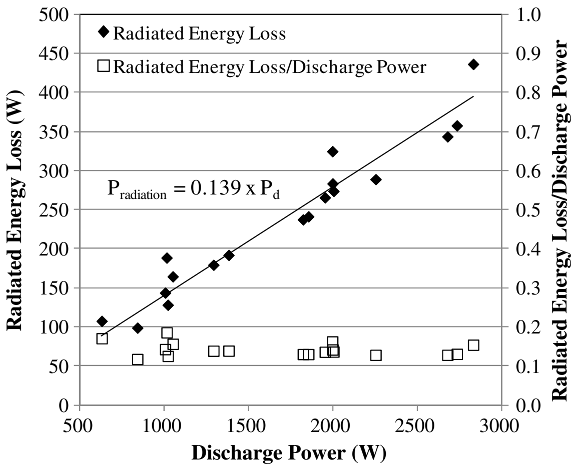

Fig. 18 Radiated power from the BN channel wall for the T-140 HET.

[22]. The data presented in Fig. 17 show energy losses to the channel wall twice as large as those measured by Shastry [22], which indicates that electron power to the walls may play a larger role then previously suggested [4,17,29]. The limited variation in the percentage of discharge power deposited into the wall from the plasma, despite improvement in plume divergence with power and voltage in HETs [21,22], also points to a large role of electron heating of the channel wall as expressed in Eq. (1). An improvement in the collimation of the plume is expected to lower the number of high-energy ions that impact the downstream half of the channel, which will lower the percentage of power deposited into the walls. Electron power peaks near the exit plane of the thruster [22] and is not affected by improvements in beam collimation. However, the calculation of electron power is sensitive to uncertainties in the measured electron temperature as well as the secondary electron emission coefficient. As pointed out by Shastry [22], a direct calculation yields large electron currents that result in incident electron powers greater than the discharge power.

It is worth noting that the energy fluxes on the downstream end of the channel are nearly 100x higher than those recorded by Mazouffre et al. using a thermal imaging camera with the 5 kW PPSX000 thruster, but power losses are similar [20]. This is likely due to the fact that the spatial resolution of the T-140 HET measurements is much better because the energy fluxes on the upstream portion of the channel agree quite well with the values reported by Mazouffre et al. [20].

D. Radiation from Boron Nitride to Environment

Radiation can be analyzed by looking at how one surface radiates to a second surface. Ideal radiation is for a blackbody and assumes that all the energy radiated by one surface goes to another surface. Because real surfaces are not blackbodies, the emissivity ε is included in the radiation calculation as a way to approximate radiation from a real body using a blackbody curve shape [31]. Emissivity essentially gives the ratio between a real and a blackbody. Real radiation is represented by the following equation:

$$\frac{q_{\mathrm{rad}}}{A} = \sigma\varepsilon(T_1^4 - T_2^4) \tag{10}$$

where σ is the Stefan–Boltzmann constant ($5.669 \times 10^{-8}\ \mathrm{W/m^2k^4}$), T_2 is taken to be the temperature of the thruster wall with just the magnets on (no discharge), and T_1 is taken to be the maximum temperature recorded on the outer wall (steady-state temperature). A value of 0.92 is used for the emissivity of the boron nitride channel [32]. The radiated energy calculations are presented in Fig. 18.

Figure 18 shows that, although the radiated power is a function of temperature, it scales linearly with discharge power. Figure 18 shows that the radiated power can be approximated as a linear function of discharge power ($0.139 \times P_d$). Mazouffre et al. calculated a value of $0.072 \times P_d$ using a thermal imaging camera [32]. The sputtering and deposition processes inherent to HET operation may cause some time-dependent fluctuation in emissivity as well as viewport transmission resulting in the lower estimate in [32]. The average radiated energy for the T-140 HET is approximately 14% of the discharge power over the entire power range tested, with excess power being measured at 125 and 150 V. The uncertainty of the percentage of the input power that is radiated away is $+4/-2\%$. These voltages correspond to the three elevated data points at approximately 1000 W and the single elevated data point at 2000 W in Fig. 18. At low voltage, the ion beam diverges more readily and relative sheath energies are higher, which results in large ion currents [22]. Radiation from the anode face, which is heated by electron current, also contributes to heating the discharge channel. A review of Fig. 4 shows that the backside of the anode nearly matches the channel temperatures. The neutral propellant temperature, which approximates the front anode face temperature, has been measured inside a HET channel with laser-induced fluorescence and shown to vary from 600 to 1600 K [33]. Given that approximately 13% of the discharge power is deposited into the discharge channel wall, whereas approximately 14% of the discharge power is radiated from the channel, radiation is the primary cooling mechanism in an HET. Next to beam power, the radiated power is the primary mechanism in which the power leaves the thruster.

VI. Conclusions

The discharge wall temperature profile of the HET is well correlated with the magnetic field profile along the wall of the discharge channel and peaks at nearly the same axial location as the peak in the magnetic field. Wall temperatures of the HET channel are primarily a function of the applied power. The radiated energy loss is approximately 14% of the discharge power over the entire power range tested. The percentage of the power from the plasma to the wall is approximately 13% over the power range tested, which illuminates radiation as the primary cooling mechanism of the channel. To reduce power deposition to the wall, the peak of the radial magnetic field should be placed downstream of the channel wall exit plane, which may lead to an increase in HET power density capability.

Acknowledgments

Support for this research is provided by Lockheed Martin. The authors would like to thank Pratt and Whitney Rocketdyne for supplying the High-Power Electric Propulsion Laboratory (HPEPL) with the T-140 HET and departmental technical staff and other graduate students at HPEPL for assistance with this work.

References

[1] Randolph, T. M., "Qualification of Commercial Electric Propulsion Systems for Deep Space Missions," *30th International Electric Propulsion Conference*, IEPC Paper 2007-271, Florence, Italy, Sept. 2007.

[2] Myers, R., and Carpenter, C., "High Power Solar Electric Propulsion for Human Space Exploration Architectures," *32nd International Electric Propulsion Conference*, IEPC Paper 2011-261, Wiesbaden, Germany, Sept. 2011.

[3] Byers, D. C., and Dankanich, J. W., "Geosynchronous-Earth-Orbit Communication Satellite Deliveries with Integrated Electric Propulsion," *Journal of Propulsion and Power*, Vol. 24, No. 6, Nov.–Dec. 2008, pp. 1369–1375.
doi:10.2514/1.35322

[4] Mazouffre, S., Dannenmayer, K., and Perez-Luna, J., "Examination of Plasma-Wall Interactions in Hall Effect Thrusters by Means of Calibrated Thermal Imaging," *Journal of Applied Physics*, Vol. 102, No. 2, 2007, pp. 023304-1–023304-10.
doi:10.1063/1.2757716

[5] Arkhipov, A. S., Kim, V., Sidorenko, E. K., and Khartov, S. A., "Analysis of Energy Balance in the Discharge of SPT Using Results of Its Integral Parameters and Plume Characteristics Measurements," *31st International Electric Propulsion Conference*, IEPC Paper 2009-097, Ann Arbor, MI, Sept. 2009.

[6] Kim, V., “Main Physical Features and Processes Determining the Performance of Stationary Plasma Thrusters,” *Journal of Propulsion and Power*, Vol. 14, No. 5, 1998, pp. 736–743. doi:10.2514/2.5335
[7] Warner, N., “Theoretical and Experimental Investigation of Hall Thruster Miniaturization,” Ph.D. Dissertation, Massachusetts Inst. of Technology, Cambridge, MA, June 2007.
[8] De Grys, K., Rayburn, C., and Haas, J., “Study of Power Loss Mechanisms in the BPT-4000 Hall Thruster,” *39th AIAA/ASME/SAE/ASEE Joint Propulsion Conference*, AIAA Paper 2003-5277, Huntsville, AL, July 2003.
[9] Goebel, D., and Katz, I., *Electric Propulsion: Ion and Hall Thrusters*, Wiley, Hoboken, NJ, 2008, pp. 347–363.
[10] Hobbs, G. D., and Wesson, J. A., “Heat Flow Through a Langmuir Sheath in the Presence of Electron Emission,” *Plasma Physics*, Vol. 9, No. 1, 1967, pp. 85–87. doi:10.1088/0032-1028/9/1/410
[11] Haas, J. M., “Low-Perturbation Interrogation of the Internal and Near-Field Plasma Structure of a Hall Thruster Using a High-Speed Probe Positioning System,” Ph.D. Dissertation, Aerospace Engineering, Univ. of Michigan, Ann Arbor, MI, 2001.
[12] Baranov, V., Nazarenko, Y., and Petrosov, V., “The Wear of the Channel Walls in Hall Thrusters,” *27th International Electric Propulsion Conference*, IEPC Paper 2001-048, Pasadena, CA, Oct. 2001.
[13] Manzella, D., “Stationary Plasma Thruster Plume Emissions,” *23rd International Electric Propulsion Conference*, IEPC Paper 1993-097, Sept. 1993.
[14] “Vacuum Measurement Catalog,” Product Catalog Varian, Inc., Vacuum Technologies, Palo Alto, CA, 2010, http://www.varianinc.com/cgi-bin/nav?products/vacuum/measure/gauges&cid=JPLHPIHFO [accessed Sept. 2009].
[15] Mclean, C. H., McVey, J. B., and Schappell, D. T., “Testing of a U.S.-Built HET System for Orbit Transfer Applications,” *35th AIAA Joint Propulsion Conference*, AIAA Paper 1999-2574, Los Angeles, CA, June 1999.
[16] Dushman, S., and Lafferty, J. M., *Scientific Foundations of Vacuum Technique*, 2nd ed., Wiley, New York, 1962, pp. 301–346.
[17] Mazouffre, S., Echegut, P., and Dudeck, M., “A Calibrated Infrared Imaging Study on the Steady State Thermal Behavior of Hall Effect Thrusters,” *Plasma Sources Science and Technology*, Vol. 16, No. 1, 2007, pp. 13–22. doi:10.1088/0963-0252/16/1/003
[18] Kim, V., Kozlov, V., Popov, G., Skrylinikov, A., Kozubsky, K., and Lyszyk, M., “Investigation of the Stationary Plasma Thruster (SPT) Outgassing and Its Thermal State Impact on Thruster Performance Variation in Time,” *26th International Electric Propulsion Conference*, IEPC Paper 1999-084, Kitakyushu, Japan, Oct. 1999.
[19] Linnell, J. A., “An Evaluation of Krypton Propellant in Hall Thrusters,” Ph.D. Dissertation, Univ. of Michigan, Ann Arbor, MI, 2007.
[20] Mazouffre, S., Dannenmayer, K., and Blank, C., “Impact of Discharge Voltage on Wall-Losses in a Hall Thruster,” *Physics of Plasmas*, Vol. 18, No. 6, 2011, pp. 064501-1–064501-4. doi:10.1063/1.3592251
[21] Xu, K., “Ion Collimation and In-Channel Potential Shaping Using In-Channel Electrodes for Hall Effect Thrusters,” Ph.D. Dissertation, Georgia Inst. of Technology, Atlanta, 2012.
[22] Shastry, R., “Experimental Characterization of the Near-Wall Region in Hall Thrusters and Its Implications on Performance and Lifetime,” Ph.D. Dissertation, Aerospace Engineering, Univ. of Michigan, Ann Arbor, MI, 2011.
[23] Staack, D., Raitses, Y., and Fisch, N. J., “Temperature Gradient in Hall Thrusters,” *Applied Physics Letters*, Vol. 84, No. 16, April 2004, pp. 3028–3030. doi:10.1063/1.1710732
[24] Katz, I., Mikellides, I. G., and Hofer, R. R., “Channel Wall Plasma Thermal Loads in Hall Thrusters with Magnetic Shielding,” *47th AIAA/ASME/SAE/ASEE Joint Propulsion Conference*, AIAA Paper 2011-6082, San Diego, CA, July–Aug. 2011.
[25] Reid, B. M., “The Influence of Neutral Flow Rate in the Operation of Hall Thrusters,” Ph.D. Dissertation, Aerospace Engineering, Univ. of Michigan, Ann Arbor, MI, 2008.
[26] Hofer, R. R., “Development and Characterization of High-Efficiency, High-Specific Impulse Xenon Hall Thrusters,” Ph.D. Dissertation, Aerospace Engineering, Univ. of Michigan, Ann Arbor, MI, 2004.
[27] Matlock, T. S., Hargus, W. A., and Larson, C. W., “Thermographic Characterization and Comparison of 200W and 600W Hall Thruster,” *43rd AIAA/ASME/SAE/ASEE Joint Propulsion Conference*, AIAA Paper 2007-5241, Cincinnati, OH, July 2007.
[28] Walter, J., and Dickens, J., “Thermal Characterization and Modeling of a Low-Power Laboratory Model TAL,” *27th International Electric Propulsion Conference*, IEPC Paper 2001-072, Pasadena, CA, Oct. 2001.
[29] Kim, V., Kozlov, V. I., Skrylnikov, A. I., Umnitsin, L. N., Svotina, V. V., Bouchoule, A., and Prioul, M., “Investigation of the Local Plasma Parameter Distribution in the SPT Accelerating Channel Under Increased Discharge Voltages,” *29th International Electric Propulsion Conference*, IEPC Paper 2005-004, Princeton Univ., NJ, Oct.–Nov. 2005.
[30] Gawron, D. D., Mazouffre, S., Albarede, L., and Sadeghi, N., “Examination of Hall Effect Thruster Acceleration Layer Characteristics by Laser Spectroscopy and Repulsing Potential Analyzer,” *42nd AIAA/ASME/SAE/ASEE Joint Propulsion Conference*, AIAA Paper 2006-4473, Sacramento, CA, July 2006.
[31] Siegel, R., and Howell, J. R., *Thermal Radiation Heat Transfer*, 3rd ed., Hemisphere Publishing Corp., Washington, D.C., 1992, pp. 41–47.
[32] Mazouffre, S., Luna, J. P., Gawron, D., Dudeck, M., and Echegut, P., “An Infrared Thermography Study on the Thermal Load Experienced by a High Power Hall Thruster,” *29th International Electric Propulsion Conference*, IEPC Paper 2005-063, Princeton Univ., NJ, Oct.–Nov. 2005.
[33] Huang, W., and Gallimore, A., “Neutral Flow Evolution in a Six-Kilowatt Hall Thruster,” *Journal of Propulsion and Power*, Vol. 27, No. 3, 2011, pp. 553–563. doi:10.2514/1.54141

L. King
Associate Editor